Intersubband polaritons at $\lambda \sim 2\,\mu\text{m}$ in the InAs/AlSb system

P. Laffaille, J.-M. Manceau, T. Laurent, A. Bousseksou, L. Le Gratiet, R. Teissier, A. N. Baranov, and R. Colombelli

Citation: Appl. Phys. Lett. **112**, 201113 (2018); doi: 10.1063/1.5023284
View online: https://doi.org/10.1063/1.5023284
View Table of Contents: http://aip.scitation.org/toc/apl/112/20
Published by the American Institute of Physics

APPLIED PHYSICS LETTERS **112**, 201113 (2018)

Intersubband polaritons at $\lambda \sim 2\,\mu$m in the InAs/AlSb system

P. Laffaille,[1] J.-M. Manceau,[1] T. Laurent,[1] A. Bousseksou,[1] L. Le Gratiet,[1] R. Teissier,[2]
A. N. Baranov,[2] and R. Colombelli[1,a)]
[1]*Centre de Nanosciences et de Nanotechnologies (C2N Orsay), CNRS UMR9001, University Paris Sud, University Paris Saclay, 91405 Orsay, France*
[2]*Institut d'Electronique et des Système (IES), University Montpellier, CNRS, 34095 Montpellier, France*

(Received 23 January 2018; accepted 21 April 2018; published online 18 May 2018)

We demonstrate intersubband polaritons at very short wavelengths, down to $\lambda \sim 2\,\mu$m, using a mature semiconductor material system InAs/AlSb and a metal-insulator-metal resonator architecture. The demonstration is given for intersubband transitions centered at 350 meV ($\lambda = 3.54\,\mu$m) and 525 meV ($\lambda = 2.36\,\mu$m). The polaritonic dispersions are measured at room-temperature and minimum splittings (Rabi splitting) of ≈50 meV are observed. We also quantitatively show that non-parabolicity effects limit the Rabi energy that can be obtained and must be crucially taken into account to correctly model these devices. Intersubband polaritons operating in the short-wave infrared region could enable the use of extremely effective pump laser sources in the quest for an intersubband polariton laser. *Published by AIP Publishing.* https://doi.org/10.1063/1.5023284

Intersubband (ISB) polaritons originate from the strong light-matter coupling between an intersubband transition (more precisely: an intersubband plasmon) in a semiconductor quantum well (QW) and a microcavity photon mode. They were first observed at mid-IR frequencies,[1] and subsequent developments targeted a variety of subjects.[2–4] In terms of frequency coverage, the extension to lower frequencies was especially targeted down to the THz[5] and sub-THz[6] ranges with the aim of reaching the ultra-strong coupling regime.[7] The extension to *higher* frequencies/*shorter* wavelengths was initially not pursued, possibly because *exciton polaritons* cover the visible and near-infrared ranges and are far more developed.[8–10]

Recently, however, the peculiar properties of the polaritonic states arising from the strong coupling of photons with intersubband plasmons have been elucidated,[11–13] and it has emerged that an ISB polaritonic system would differ substantially from an exciton polariton system operating at the same wavelength. On one hand, the bosonic character of exciton polaritons is lost above the Mott transition. This has important consequences for exciton polariton lasers: it sets an intrinsic upper limit to the available output power, and also to the maximum operating temperature. On the contrary, ISB polaritons are free from this strict limit to their bosonicity.[13] On the other hand, once the ultra-strong coupling regime is achieved, the anti-resonant terms of the Hamiltonian become non-negligible: intriguing quantum electrodynamics (QED) phenomena arise.[14] However, the ultra-strong coupling regime was originally demonstrated at THz frequencies, a spectral region that lacks detectors suitable for QED studies. Operating at shorter wavelengths, where single-photon detectors are available, is clearly better. For all these reasons, it is useful to extend the concept of ISB polaritons to short IR wavelengths. To date, demonstrations of ISB polaritons in the 1.5–3 μm wavelength range have been based on the GaN/Al(Ga)N system.[15,16] This system enjoys a very large conduction band offset,[17] but it is not as advanced as other III-V materials in terms of maturity.

In this letter, we demonstrate ISB polaritons at very short infrared wavelengths using a mature semiconductor material system such as InAs/AlSb, that has been successfully exploited in the past to develop short-IR quantum cascade (QC) lasers,[18] and also for ISB polaritons in the mid-IR spectral range.[19] Using dispersive metal-semiconductor-metal resonators[20] and InAs/AlSb QWs exhibiting ISB transitions centered at 350 meV ($\lambda = 3.54\,\mu$m) and 525 meV ($\lambda = 2.36\,\mu$m), we provide evidence of ISB polaritons down to $\lambda = 2\,\mu$m. We also highlight that—in order to correctly design short-wavelength polaritonic devices in this system—non-parabolicity effects must be carefully taken into account.

The two semiconductor structures employed are described below. Structure C231 consists of 23 repetitions of 5.9-nm-thick InAs QWs, separated by 5 nm AlSb barriers. The QWs are n-doped with Si at 2.5×10^{18} cm^{-3}, that makes a sheet doping density of 1.48×10^{12} cm^{-2} per QW. Structure EQ247 consists of 20 repetitions of 3.6-nm-thick InAs QWs, separated by 5 nm AlSb barriers. The QWs are n-doped with Si at 1.56×10^{19} cm^{-3}, that makes a sheet doping density of 5.62×10^{12} cm^{-2} per QW. Both samples have been grown on InAs substrates followed by a special multiple etch-stop layer sequence to efficiently perform substrate removal, as described in Ref. 21.

Figure 1 presents the band diagram of the two structures (one period) calculated with a Schrödinger-Poisson solver. The QWs in sample C231 have 3 confined states, and the calculated energy of the 1→2 transition is $\overline{E}_{12} = \sqrt{E_{12}^2 + E_{plasma}^2} = 335$ meV ($\lambda = 3.7\,\mu$m). The nominal E_{12} is 324.5 meV and E_{plasma} is 83 meV. With regards to sample EQ247, that was designed to exhibit a shorter wavelength transition, we calculate $\overline{E}_{12} =$ 534.5 meV ($\lambda = 2.32\,\mu$m). The position of the Fermi level for the two samples is also marked in Fig. 1.

In both samples, the energy of the 1→2 transition is close to or larger than the InAs substrate energy gap. This makes the measurement of the ISB transition *via* a multipass

---

[a] E-mail: raffaele.colombelli@u-psud.fr

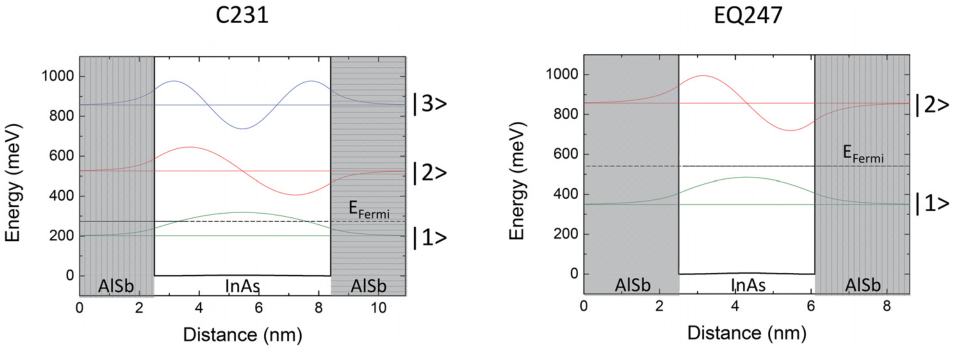

FIG. 1. Conduction band electronic structure of the two samples studied. The electronic wavefunctions are plotted. The effect of doping is introduced with a Schrödinger-Poisson approach. The respective Fermi levels are marked by the dashed horizontal lines.

waveguide technique impossible. We have therefore employed an attenuated-total-reflection (ATR) technique as sketched in the lower-left inset of Fig. 2. The samples have been waferbonded to a GaAs host wafer using standard gold-gold thermo-compression techniques, followed by the initial substrate and stop layer removal with citric acid and an HCl-based solution, respectively.[21] Figure 2 (main panel) reports the reflectivity of sample C231 measured in an ATR configuration at room-temperature. The spectra in this paper are typically measured using a Fourier transform infrared (FTIR) spectrometer. The FTIR internal globar lamp is employed as a source, and detection is performed with the internal Mercury-Cadmium-Telluride (MCT) or internal deuterated triglycine sulfate (DTGS) detector. An absorption peak centered at $\overline{E}_{12} = 346.7$ meV is observed, in fair agreement with the simulations. The asymmetric line shape, with a low-energy tail, stems from strong non-parabolicity effects. The lower right inset of Fig. 2 reports the calculated electronic effective mass at a temperature of 300 K in an InAs/AlSb QW as a function of the electron energy relative to the bottom of the conduction band. At energies of 200 and 525 meV that correspond to the first two subbands of sample C231, the effective mass is, respectively, 0.049 and 0.097, far from the usually used InAs effective mass of 0.023, valid at the bottom of the conduction band at low temperature.

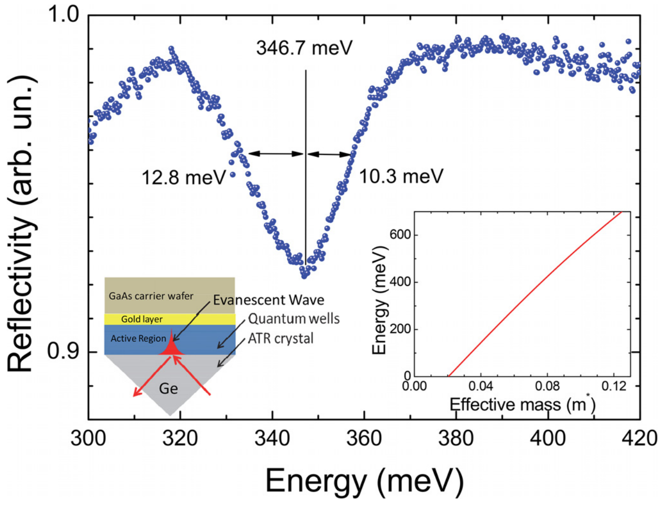

FIG. 2. Attenuated total reflectivity measurement on sample C231 (the material used as the ATR crystal is germanium). The measurement scheme is shown in the lower left inset. The measurement is the ratio between the reflectivity on the sample and the reflectivity on an identical one, but with undoped QWs (reference sample). The lower right inset shows the calculated relation between the effective mass and electron energy relative to the bottom of the conduction band.

We have then inserted the two samples into dispersive, grating-based metal-dielectric-metal resonators—as sketched in the inset of Fig. 3(a)—following the procedure described in Ref. 20. This geometry permits to easily perform reflectivity measurements and extract the device photonic band structure, that is reported in Fig. 3(a). A clear anti-crossing between the cavity mode and the ISB plasmon (blue dashed horizontal line) is observed. This choice of grating and the filling factor (*ff*, the ratio between the width of the metallic fingers and the grating period) place the anticrossing at $\frac{\Delta k_\parallel}{\pi} \approx 0.3$, and the shortest measured polariton frequency, at room temperature, for an incidence angle of 73° is 3.2 μm (387 meV).

As discussed in Ref. 20, the system can be modeled using Rigorous Coupled Wave Analysis (RCWA) simulations, in combination with an effective dielectric function that models the active region following the Załuzny–Nalewajko approach described in Ref. 23. The numerical results are reported in Fig. 3(b), where the standard $m^* = 0.023$ for InAs is employed: they fail to reproduce the experimental results of Fig. 2(a).

To take into account the non-parabolicity, we incorporate the non-normalized oscillator strength $\tilde{f}_{12}$ between the first two subbands in the expression of the z-component of the effective permittivity tensor (as described in Ref. 22) where

$\tilde{f}_{12}$ is defined as

$$\tilde{f}_{12} = \frac{m_0}{2E_{12}} \left| \left\langle 2 \middle| \boldsymbol{p}_z \frac{1}{m(E_1)} + \frac{1}{m(E_2)} \boldsymbol{p}_z \middle| 1 \right\rangle \right|^2, \tag{1}$$

and the permittivity tensor is defined as

$$\varepsilon_z(\omega) = \varepsilon_\infty \left(1 - \frac{\varepsilon_\infty^2}{\varepsilon_{well}^2} \frac{\omega_p^2}{\omega_{12}^2 - \omega^2 - i\omega\Gamma_{12}} \right)^{-1}, \tag{2}$$

$$\text{with} \quad \omega_p = \sqrt{\frac{\pi e^2 n_{2D} \tilde{f}_{12}}{\varepsilon_\infty m_0 (L_b + L_w)}}, \tag{3}$$

where p_z is the operator momentum along the growth axis, Γ_{12} is the FWHM of the ISB transition, $\varepsilon_{\text{well}}$ is the dielectric constant of the well material, m_0 is the free electron mass, L_b and L_w are, respectively, the barrier and well thicknesses, and n_{2D} stands for the dopants' concentration. For sample C231, we numerically calculate $\tilde{f}_{12} = 13.1$. The results of this approach are reported in Fig. 3(c): taking the non-parabolicity

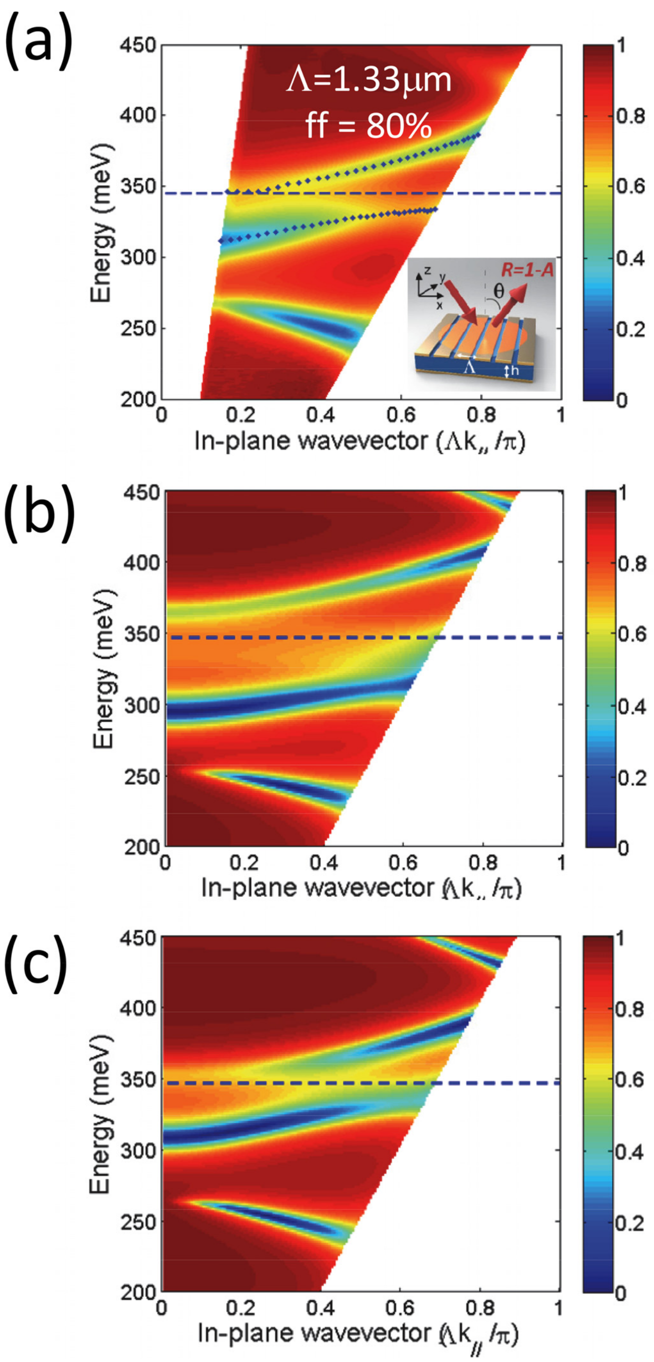

FIG. 3. (a) Experimental polaritonic dispersion of sample C231. The measurement geometry is reported in the inset, and more details can be found in Ref. 20. The lowest incidence angle is 13°, while the highest is 73°. The grating period is 1330 nm and the filling factor (ff) is 80%. The grating was fabricated by electron beam lithography, followed by deposition of Ti/Au layers. The polariton peaks are marked by dots, while the bare ISB transition corresponds to the dashed horizontal line. A Rabi splitting of approx. 36 meV is obtained. (b) Calculated polaritonic dispersion of sample C231 without taking into account non-parabolicity effects: the Rabi splitting is largely over-estimated. (c) Calculated polaritonic dispersion with the inclusion of the non-parabolicity effects: the agreement with the experiments is excellent.

into account permits to perfectly reproduce the experimental findings.

On sample EQ247, it was not possible to measure the ISB transition with ATR, since we did not have a reference undoped sample in this case. Nevertheless, we have implemented a grating-based resonator on sample EQ247 using as a target the nominal ISB transition energy $\overline{E}_{12}$=534.5 meV ($\lambda = 2.32\,\mu$m). The experimental, room-temperature photonic band-structure, extracted from the angle-resolved reflectivity, is reported in Fig. 4(a): an anti-crossing is visible between the ISB plasmon—that appears to be at $\overline{E}_{12} = 525$ meV—and the photonic mode. The shortest measured polariton wavelength—for an incidence angle of 67°—is $\lambda = 2.03\,\mu$m. We have simulated the system with an RCWA approach using the

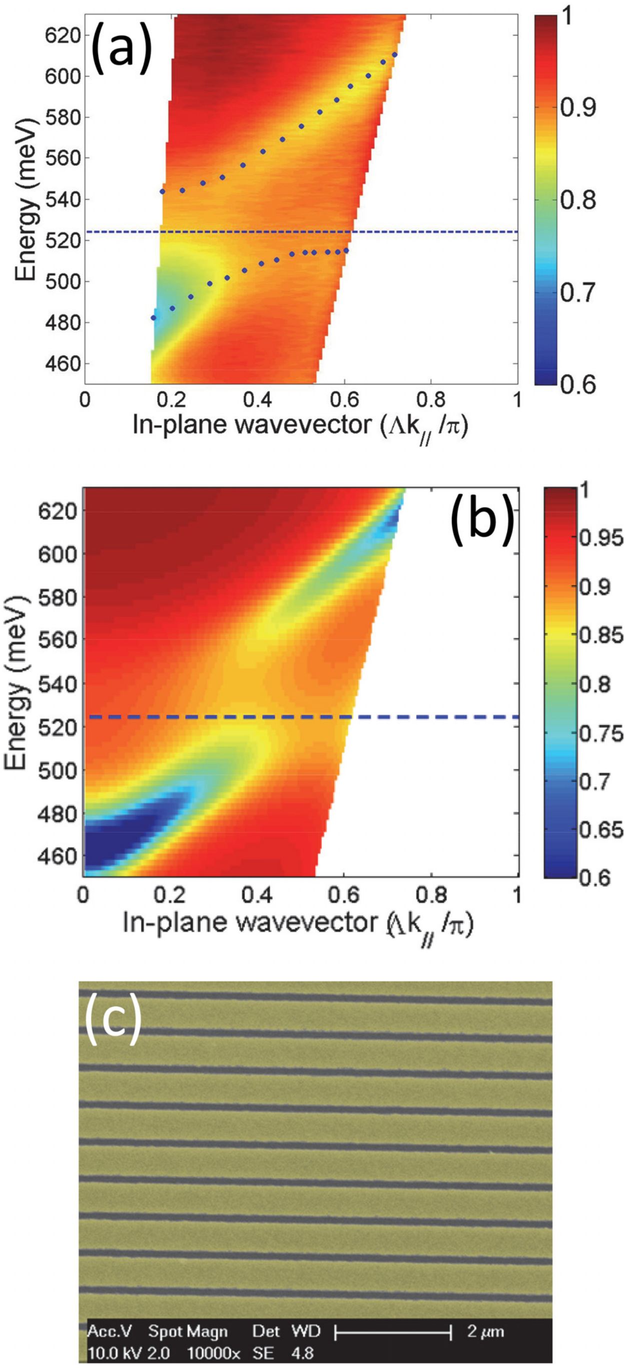

FIG. 4. (a) Experimental polaritonic dispersion of sample EQ247. The measurement geometry is similar to the previous sample. The grating period is 790 nm and *ff* is 93%. The polariton peaks are marked by dots, while the estimated ISB transition corresponds to the dashed horizontal line. For an estimated ISB wavelength of 2.32 μm, the longest wavelength attained by the lower-polariton is 2.58 μm, while the shortest wavelength (upper polariton) is 2.03 μm. (b) Calculated polaritonic dispersion with the inclusion of the non-parabolicity effects: the agreement with the experiments is excellent. (c) Colored SEM image of a typical grating.

nominal sample parameters, an ISB transition energy of 525 meV and a $\tilde{f}_{12}$ value of 8.06, taking into account the non-parabolicity. The results are reported in Fig. 4(b): the agreement with the experimental results is excellent. It also confirms that sample EQ247 features an ISB transition at $\lambda = 2.36\,\mu$m, in good agreement with the nominal value of 2.32 μm.

The minimum splitting (Rabi splitting, $2\Omega_{\mathrm{Rabi}}$) obtained with sample C231 is 36 meV, while with sample EQ247, it is 53 meV. The ratio between the two is 1.47. It is possible to theoretically estimate the ratio between the splittings, as the following formula is valid:

$$2\Omega_{\mathrm{Rabi}} = \sqrt{\Gamma \cdot \mathrm{f_w}}\Omega_{\mathrm{plasma}} \propto \sqrt{\mathrm{n_{2D}} \cdot \mathrm{f_w} \cdot \tilde{f}_{12}},$$

where Γ is the electromagnetic confinement factor, here, essentially equal to 1; $\mathrm{f_w}$ is the mode optical confinement factor (defined as the ratio between the sum of the thickness of all the QWs and the total sample thickness); and $\mathrm{n_{2D}}$ is the surface charge density per QW. Each QW of sample C231 is nominally n-doped at 1.48×10^{12} cm^{-2}, while sample EQ247 is n-doped at 5.6×10^{12} cm^{-2}. Using the nominal sample values, and importantly, the effective mass change because of the non-parabolicity, we obtain a ratio of 1.45. This is in good agreement with the experiment and it further confirms that non-parabolicity effects must be included while designing InAs/AlSb polaritonic samples for short-IR wavelengths, especially if we target large Rabi splittings.

In conclusion, we have reported intersubband polaritons at very short wavelengths, down to $\lambda \sim 2\,\mu$m, using a mature semiconductor material system such as InAs/AlSb and a metal-insulator-metal resonator architecture. On one hand, this result shows that InAs/AlSb can be effectively used to develop ISB polaritonic devices well into the InAs interband absorption region: 2 μm represents one of the shortest wavelengths ever achieved in this system. On the other hand, achieving very large Rabi splitting becomes more and more difficult, given the non-parabolicity effects that affect the plasma frequency. However, Rabi splitting larger than or equal to the longitudinal optical phonon in InAs is easily achievable; therefore, this system can be used to explore ISB polariton-LO phonon scattering processes that are crucial to the operation of a perspective ISB polariton laser.

This work was partly supported by the French RENATECH network. We acknowledge financial support from the European Research Council (IDEASERC) ("GEM") (306661) and from the FET-Open grant "MIR-BOSE" (Grant Agreement 737017). Part of this work was supported by the French program on "Investments for the Future" [EquipEx EXTRA (ANR-11-EQPX-0016)].

[1] D. Dini, R. Köhler, A. Tredicucci, G. Biasiol, and L. Sorba, Phys. Rev. Lett. **90**, 116401 (2003).
[2] L. Sapienza, A. Vasanelli, R. Colombelli, C. Ciuti, Y. Chassagneux, C. Manquest, U. Gennser, and C. Sirtori, Phys. Rev. Lett. **100**, 136806 (2008).
[3] R. Colombelli, C. Ciuti, Y. Chassagneux, and C. Sirtori, Semicond. Sci. Technol. **20**, 985 (2005).
[4] G. Günter, A. A. Anappara, J. Hees, A. Sell, G. Biasiol, L. Sorba, S. De Liberato, C. Ciuti, A. Tredicucci, A. Leitenstorfer, and R. Huber, Nature **458**, 178 (2009).
[5] Y. Todorov, A. M. Andrews, I. Sagnes, R. Colombelli, P. Klang, G. Strasser, and C. Sirtori, Phys. Rev. Lett. **102**, 186402 (2009).
[6] G. Scalari, C. Maissen, D. Turčinková, D. Hagenmüller, S. De Liberato, C. Ciuti, C. Reichl, D. Schuh, W. Wegscheider, M. Beck, and J. Faist, Science **335**, 1323 (2012).
[7] C. Ciuti and I. Carusotto, Phys. Rev. A **74**, 33811 (2006).
[8] C. Weisbuch, M. Nishioka, A. Ishikawa, and Y. Arakawa, Phys. Rev. Lett. **69**, 3314 (1992).
[9] D. Bajoni, J. Phys. D Appl. Phys. **45**, 313001 (2012).
[10] J. Kasprzak, M. Richard, S. Kundermann, A. Baas, P. Jeambrun, J. M. J. Keeling, F. M. Marchetti, M. H. Szymańska, R. André, J. L. Staehli, V. Savona, P. B. Littlewood, B. Deveaud, and L. S. Dang, Nature **443**, 409 (2006).
[11] S. De Liberato, C. Ciuti, and I. Carusotto, Phys. Rev. Lett. **98**, 103602 (2007).
[12] S. De Liberato and C. Ciuti, Phys. Rev. Lett. **102**, 136403 (2009).
[13] R. Colombelli and J.-M. Manceau, Phys. Rev. X **5**, 11031 (2015).
[14] C. Ciuti, G. Bastard, and I. Carusotto, Phys. Rev. B **72**, 115303 (2005).
[15] A. Benz, S. Campione, M. W. Moseley, J. J. Wierer, A. A. Allerman, J. R. Wendt, and I. Brener, ACS Photonics **1**, 906 (2014).
[16] T. Laurent, J. M. Manceau, E. Monroy, C. B. Lim, S. Rennesson, F. Semond, F. H. Julien, and R. Colombelli, Appl. Phys. Lett. **110**, 131102 (2017).
[17] H. Machhadani, P. Kandaswamy, S. Sakr, A. Vardi, A. Wirtmüller, L. Nevou, F. Guillot, G. Pozzovivo, M. Tchernycheva, A. Lupu, L. Vivien, P. Crozat, E. Warde, C. Bougerol, S. Schacham, G. Strasser, G. Bahir, E. Monroy, and F. H. Julien, New J. Phys. **11**, 125023 (2009).
[18] A. N. Baranov and R. Teissier, IEEE J. Sel. Top. Quantum Electron. **21**, 85 (2015).
[19] A. A. Anappara, D. Barate, A. Tredicucci, J. Devenson, R. Teissier, and A. Baranov, Solid State Commun. **142**, 311 (2007).
[20] J.-M. Manceau, S. Zanotto, T. Ongarello, L. Sorba, A. Tredicucci, G. Biasiol, and R. Colombelli, Appl. Phys. Lett. **105**, 81105 (2014).
[21] D. Chastanet, A. Bousseksou, G. Lollia, M. Bahriz, F. H. Julien, A. N. Baranov, R. Teissier, and R. Colombelli, Appl. Phys. Lett. **105**, 111118 (2014).
[22] C. Sirtori, F. Capasso, J. Faist, and S. Scandolo, Phys. Rev. B **50**, 8663 (1994).
[23] M. Załużny and C. Nalewajko, Phys. Rev. B **59**, 13043 (1999).